

ANALYTIC SOLUTIONS OF THE NONLINEAR OMEGA AND VORTICITY EQUATIONS FOR A STRUCTURALLY SIMPLE MODEL OF DISTURBANCES IN THE BAROCLINIC WESTERLIES

FREDERICK SANDERS

Department of Meteorology, Massachusetts Institute of Technology, Cambridge, Mass.

ABSTRACT

Exact solutions of the nonlinear quasi-geostrophic omega and vorticity equations yield three-dimensional fields of vertical motion and geopotential tendency for a structurally simple model of cyclonic and anticyclonic disturbances in the baroclinic westerlies. Information derived from these fields is consistent in many respects with the results of classical analyses of baroclinic instability, but is more detailed. The present results seem entirely reasonable synoptically. New findings are (1) that in most instances a surface cyclone should move to the right (and an anticyclone to the left) of the upper flow over the center and (2) that the rate of deepening provided by the present physical theory probably does not account for observed instances of explosive cyclogenesis.

CONTENTS

1. Introduction.....	393
2. Structural model.....	394
3. Field of vertical motion.....	395
4. Field of geopotential tendency.....	398
5. Motion of geopotential features.....	399
6. Intensification of geopotential features.....	402
7. Field of temperature tendency.....	404
8. Concluding comments.....	407
Acknowledgments.....	407
References.....	407

1. INTRODUCTION

In textbook treatments of the structure and dynamics of extratropical cyclones and anticyclones, assumptions are often numerous, arguments often qualitative, and explanations often partial (e.g., Willett and Sanders 1959, pp. 256-259; Petterssen 1956, pp. 320-329). These considerations can be supported by numerical calculations for particular synoptic cases, but these are tedious to prepare and lack generality.

Here, we wish to follow a middle path. That is, we will show that a wealth of realistic diagnostic information can be obtained from a structurally simple model of the temperature and geopotential fields with rather few assumptions. Specifically, we will obtain analytic solutions for the three-dimensional fields of vertical motion and geopotential tendency, which are interesting in themselves and permit quantitative determination of the rates of displacement and of intensification of significant features of the geopotential and temperature fields. The relationship of these fields and rates to the basic structural parameters of the model is often quite explicit. As an illustrative case, we shall obtain the model parameters from the situation of Mar. 26, 1970, shown in figure 1 and denoted as case C.

We assume that the flow is governed by the quasi-geostrophic vorticity equation

$$\frac{\partial \zeta}{\partial t} = -\mathbf{V} \cdot \nabla \eta + \eta_0 \frac{\partial \omega}{\partial p} \tag{1}$$

and by the thermodynamic equation

$$\frac{\partial}{\partial t} \frac{\partial \phi}{\partial p} = -\mathbf{V} \cdot \nabla \frac{\partial \phi}{\partial p} - \sigma(p) \omega \tag{2}$$

where η_0 is a constant value of $\zeta + f$, the absolute vorticity; ϕ is the geopotential; and the stability parameter $\sigma(p) \equiv (d\phi/dp) (d \ln \theta/dp)$ is a function only of pressure. When the geostrophic relationship is used to express the vorticity,

$$\zeta = \nabla^2 \phi / f_0;$$

and eq (1) becomes

$$\nabla^2 \frac{\partial \phi}{\partial t} = -f_0 \mathbf{V} \cdot \nabla \eta + f_0 \eta_0 \frac{\partial \omega}{\partial p} \tag{3}$$

Here, f_0 is a constant value of the Coriolis parameter. When eq (3) and (2) are combined to eliminate $\partial \phi / \partial t$, we obtain the omega equation

$$\left(\nabla^2 + \frac{f_0 \eta_0}{\sigma} \frac{\partial^2}{\partial p^2} \right) \omega = \frac{f_0}{\sigma} \frac{\partial}{\partial p} (\mathbf{V} \cdot \nabla \eta) - \frac{1}{\sigma} \nabla^2 \left(\mathbf{V} \cdot \nabla \frac{\partial \phi}{\partial p} \right) \tag{4}$$

which has been widely discussed in this form or in related, simplified versions. The solution of this equation yields values of $\partial \omega / \partial p$, which enable a solution of eq (3) for the field of geopotential tendency. We shall obtain such solutions for the structurally simple model.

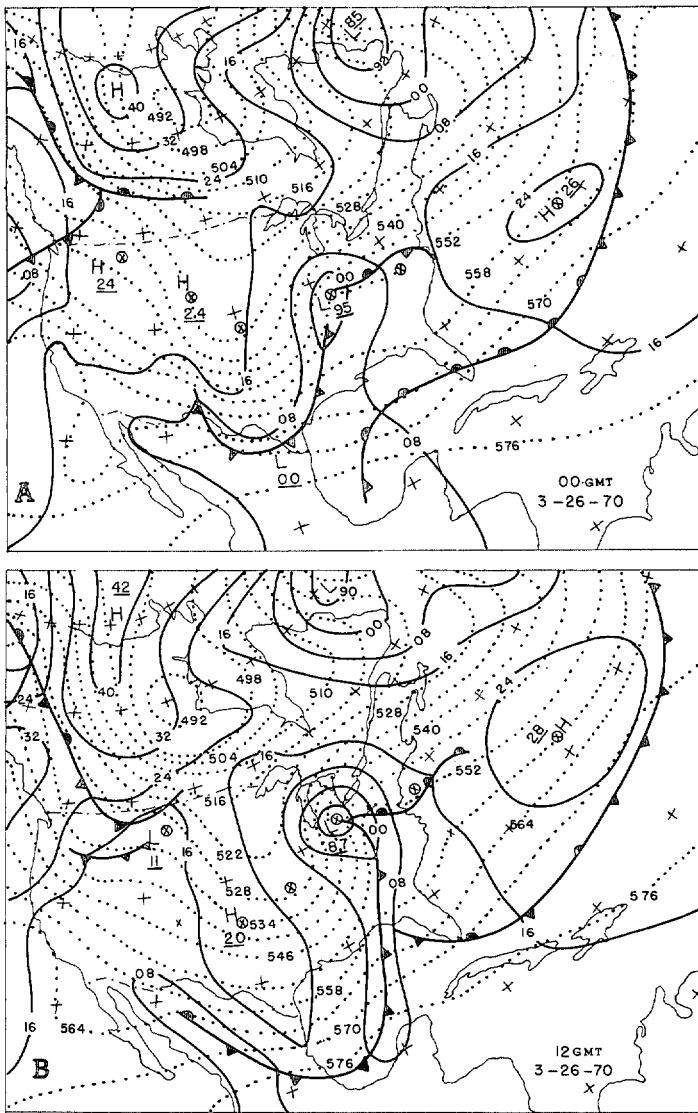


FIGURE 1.—Surface maps for (A) 0000 GMT and (B) 1200 GMT on Mar. 26, 1970. The dashed lines are isopleths of thickness of the layer from 1000 to 500 mb and are labeled in dekameters. Sea-level isobars are labeled in millibars. The encircled crosses denote the positions of perturbation centers of temperature and 1000-mb height, used as a basis for estimating the model parameters.

2. STRUCTURAL MODEL

Aiming for a maximum of flexibility and realism without paying an excessive price in the form of mathematical complexity, we assume the following structure of the temperature field:

$$T(x, y, p) = T_m(p) - \left(1 - \alpha \ln \frac{1000}{p}\right) \times \left(ay + \hat{T} \cos \frac{2\pi}{L} x \cos \frac{2\pi}{L} y\right) \quad (5)$$

where the x and y axes are directed eastward and northward, respectively; pressure is expressed in millibars; and the base of the model atmosphere is the 1000-mb level. We use the β -plane approximation. This model temperature field at 1000 mb for case C is shown in figure 2. The vertical structure of the temperature perturbation

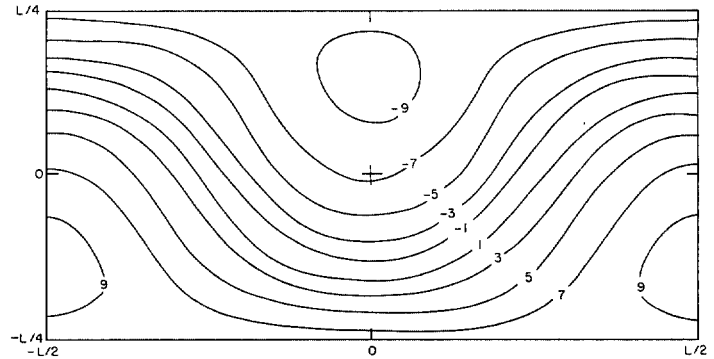


FIGURE 2.—Case C 1000-mb isotherms at intervals of 2°C, labeled as departure from map average. The values of parameters are $\alpha = 1.12 \times 10^{-5} \text{ }^\circ\text{C} \cdot \text{m}^{-1}$, $T = 7.25 \text{ }^\circ\text{C}$, and $L = 2900 \text{ km}$.

is governed by the factor, $1 - \alpha \ln(1000/p)$, which allows for damping with elevation and reversal of sign at a pressure level determined by the value of α , simulating the effect of the tropopause. The reversed perturbation becomes unrealistically large near the top of the atmosphere, but the effects of this artificiality are probably small in the lower troposphere. When $\alpha = 0.722$, the tropopause reversal occurs at the 250-mb level, as in middle latitudes in the real atmosphere, while the strength of the temperature perturbation at 500 mb drops to one-half its 1000-mb value. This decrease through the troposphere seems fairly representative of continental conditions, but is excessive for maritime regions, in which there appears to be little change in the intensity of horizontal temperature contrasts through much of the troposphere. However, the benefit of a more realistic vertical variation than that used in eq (5) is probably smaller than the cost of the additional mathematical complexity.

Since the stability factor σ is independent of x and y , it will be associated with T_m , the average over a wavelength in x and y on a constant-pressure surface. It follows from the definitions of σ and of potential temperature θ and from the hydrostatic equation that

$$\frac{d \ln \theta}{dp} = \left(\frac{d \ln T}{dp} - \frac{\kappa}{p}\right)$$

and

$$\sigma = \left(\frac{\kappa}{p} \frac{d \ln T_m}{dp}\right) \frac{RT_m}{p}$$

where κ is the ratio of the gas constant for dry air to the specific heat at constant pressure. Let us define

$$\gamma \equiv \kappa - p \frac{d \ln T_m}{dp}$$

It is evident that $\gamma = \kappa$ corresponds to an isothermal lapse rate, while $\gamma = 0$ is easily shown to correspond to a dry-adiabatic lapse rate. We will regard γ as independent of pressure, thus underestimating the stability in the stratosphere, where the model becomes unrealistic anyway. We will also adopt a constant value of temperature, T_0 , where it appears as a coefficient in the expression for σ ,

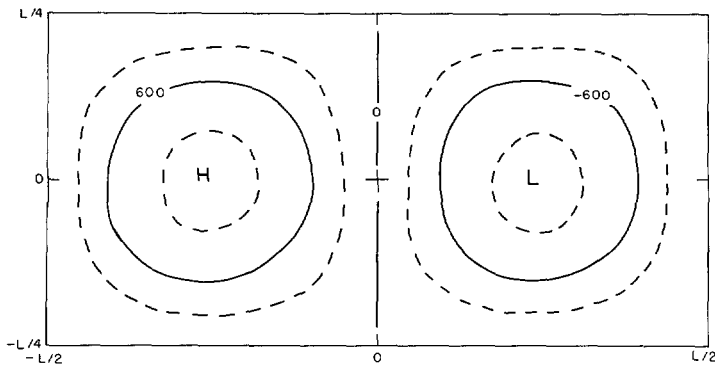


FIGURE 3.—Case C isopleths of 1000-mb geopotential at intervals of $600 \text{ m}^2\text{-s}^{-2}$. The values of parameters are $\hat{\phi}_{10} = 1020 \text{ m}^2\text{-s}^{-2}$ and $\lambda = 0.25L$.

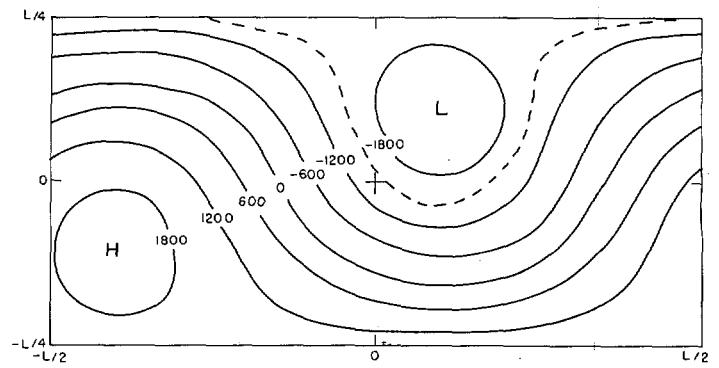


FIGURE 4.—Case C isopleths of 300-mb geopotential at intervals of $600 \text{ m}^2\text{-s}^{-2}$, labeled as departures from map-average value. The value of α is 0.722.

so that

$$\sigma(p) = RT_0\gamma/p^2. \quad (6)$$

At 1000 mb, we assume the simple distribution of geopotential given by

$$\phi(x, y, 1000) = \hat{\phi}_{10} \cos \frac{2\pi}{L}(x + \lambda) \cos \frac{2\pi}{L}y \quad (7)$$

where λ is the phase lag of the 1000-mb geopotential field relative to the temperature field. It is measured westward either from the high temperature perturbation center to the 1000-mb Low center or from the cold center to the 1000-mb High center. Thus, $\lambda = 0$ corresponds to a system of warm Lows and cold Highs while $\lambda = L/2$ yields cold Lows and warm Highs. A sample pattern for our selected case with $\lambda = L/4$, representing the typical intensifying situation in the real atmosphere, is shown in figure 3. Note that the "map average" value of $\hat{\phi}_{10}$ is arbitrarily set equal to zero.

In this model, the 1000-mb geopotential centers and the centers of the temperature perturbations are at a common latitude. In the real atmosphere, we often observe approximately this alinement, particularly while the disturbance is intensifying; but in the later stages of development, the surface cyclone tends to move to the north of the temperature perturbation centers, while the anticyclone drifts to the south.

At pressure levels above the 1000-mb level, the geopotential field is found by hydrostatic integration. Thus,

$$\begin{aligned} \phi(x, y, p) &= \phi(x, y, 1000) + \int_{1000}^p \frac{\partial \phi}{\partial p}(x, y, p) dp \\ &= \phi_m(p) + \hat{\phi}_{10} \cos \frac{2\pi}{L}(x + \lambda) \cos \frac{2\pi}{L}y \\ &\quad - \left[R \ln \frac{1000}{p} - (R\alpha/2) \left(\ln \frac{1000}{p} \right)^2 \right] \\ &\quad \times \left(ay + \hat{T} \cos \frac{2\pi}{L}x \cos \frac{2\pi}{L}y \right) \end{aligned} \quad (8)$$

where

$$\phi_m(p) = R \int_p^{1000} T_m(p) d \ln p$$

is the map-average value of $\phi(p)$. The field at 300 mb for case C is shown in figure 4. The transition from the lower to the upper level is quite realistic.

3. FIELD OF VERTICAL MOTION

We must first evaluate the forcing function of eq (4) for the structural model described above. Geostrophically,

$$\mathbf{v} = \frac{1}{f_0} \left(-\frac{\partial \phi}{\partial y} \mathbf{i} + \frac{\partial \phi}{\partial x} \mathbf{j} \right)$$

and

$$\eta = \frac{\nabla^2 \phi}{f_0} + f.$$

From these relationships and from eq (6) and (8), the omega eq (4) becomes

$$\begin{aligned} &\left(\nabla^2 + \frac{f_0 \eta_0 p^2}{RT_0 \gamma} \frac{\partial^2}{\partial p^2} \right) \omega \\ &= \left\{ \frac{4(2\pi/L)^3 Ra \hat{T}}{f_0 T_0 \gamma} p \left(\ln \frac{1000}{p} \right) \left(1 - \alpha \ln \frac{1000}{p} \right) \right. \\ &\quad \times \left(1 - \frac{\alpha}{2} \ln \frac{1000}{p} \right) - \frac{(2\pi/L) \hat{T} (\partial f / \partial y)_0}{T_0 \gamma} p \left(1 - \alpha \ln \frac{1000}{p} \right) \left. \right\} \\ &\quad \times \sin \frac{2\pi}{L}x \cos \frac{2\pi}{L}y - \frac{4(2\pi/L)^3 a \hat{\phi}_{10}}{f_0 T_0 \gamma} p \left(1 - \alpha \ln \frac{1000}{p} \right) \\ &\quad \times \sin \frac{2\pi}{L}(x + \lambda) \cos \frac{2\pi}{L}y + \frac{2(2\pi/L)^4 \hat{\phi}_{10} \hat{T} \sin(2\pi\lambda/L)}{f_0 T_0 \gamma} p \\ &\quad \times \left(1 - \alpha \ln \frac{1000}{p} \right) \sin \frac{4\pi}{L}y. \end{aligned} \quad (9)$$

It is interesting to trace the identity of the various parts of the right side of eq (9). The lengthy first term represents the effect of vorticity advection in that part of the flow attributable hydrostatically to the temperature field, the first part referring to advection of relative vorticity and the second to advection of earth vorticity. The second term is composed of two identical contributions, one from advection of the part of the relative vorticity due to the 1000-mb geopotential field by the part of the flow due to the mean meridional temperature gradient and the other from advection of this temperature gradient by

the part of the flow due to the 1000-mb geopotential field. The third term represents the effect of advection of the perturbed part of the temperature field by the part of the flow attributable to the 1000-mb geopotential field. The first term vanishes at the "longitude" of the temperature perturbation centers, while the second is similarly phased, but with respect to the 1000-mb geopotential centers. The third term is independent of x and vanishes at the "latitude" of the 1000-mb centers.

The solution of this equation is less unwieldy and perhaps more meaningful if it is undertaken piecemeal. That is, let

$$\omega = \omega_1 + \omega_2 + \omega_3 \quad (10)$$

where

$$\begin{aligned} \left(\nabla^2 + \frac{f_0 \eta_0 p^2 \partial^2}{RT_{0\gamma} \partial p^2} \right) \omega_1 = & \left\{ \frac{4(2\pi/L)^3 Ra \hat{T}}{f_0 T_{0\gamma}} p \left(\ln \frac{1000}{p} \right) \right. \\ & \times \left(1 - \alpha \ln \frac{1000}{p} \right) \left(1 - \frac{\alpha}{2} \ln \frac{1000}{p} \right) \\ & \left. - \frac{(2\pi/L) \hat{T} (\partial f / \partial y)_0}{T_{0\gamma}} p \left(1 - \alpha \ln \frac{1000}{p} \right) \right\} \\ & \times \sin \frac{2\pi}{L} x \cos \frac{2\pi}{L} y, \quad (11a) \end{aligned}$$

$$\begin{aligned} \left(\nabla^2 + \frac{f_0 \eta_0 p^2 \partial^2}{RT_{0\gamma} \partial p^2} \right) \omega_2 = & - \frac{4(2\pi/L)^3 a \hat{\phi}_{10}}{f_0 T_{0\gamma}} p \left(1 - \alpha \ln \frac{1000}{p} \right) \\ & \times \sin \frac{2\pi}{L} (x + \lambda) \cos \frac{2\pi}{L} y, \quad (11b) \end{aligned}$$

and

$$\begin{aligned} \left(\nabla^2 + \frac{f_0 \eta_0 p^2 \partial^2}{RT_{0\gamma} \partial p^2} \right) \omega_3 = & \frac{2(2\pi/L)^4 \hat{\phi}_{10} \hat{T} \sin(2\pi\lambda/L)}{f_0 T_{0\gamma}} \\ & \times p \left(1 - \alpha \ln \frac{1000}{p} \right) \sin \frac{4\pi}{L} y. \quad (11c) \end{aligned}$$

Taking the first of these equations, we require ω_1 to vanish in the horizontal where the forcing function vanishes. Thus, we are led to

$$\omega_1 = \hat{\omega}_1(p) \sin \frac{2\pi}{L} x \cos \frac{2\pi}{L} y$$

from which

$$\nabla^2 \omega_1 = -2(2\pi/L)^2 \omega_1 = -2(2\pi/L)^2 \hat{\omega}_1 \sin \frac{2\pi}{L} x \cos \frac{2\pi}{L} y,$$

so that eq (11a) becomes

$$\begin{aligned} \left[\frac{f_0 \eta_0 p^2 \partial^2}{RT_{0\gamma} \partial p^2} - 2(2\pi/L)^2 \right] \omega_1 = & \frac{4(2\pi/L)^3 Ra \hat{T}}{f_0 T_{0\gamma}} p \left(\ln \frac{1000}{p} \right) \\ & \times \left(1 - \alpha \ln \frac{1000}{p} \right) \left(1 - \frac{\alpha}{2} \ln \frac{1000}{p} \right) \\ & - \frac{(2\pi/L) \hat{T} (\partial f / \partial y)_0}{T_{0\gamma}} p \left(1 - \alpha \ln \frac{1000}{p} \right). \quad (12) \end{aligned}$$

We require, as further boundary conditions, ω to vanish at the base and at the top of the atmosphere. The same

conditions apply to ω_1 and thus to $\hat{\omega}_1$ because there will be values of x and y at which ω_1 is the only nonzero component of ω . The solution of eq (12), subject to these boundary conditions, can be written as

$$\hat{\omega}_1 = K_{11}^\omega P_{11}^\omega + K_{12}^\omega P_{12}^\omega \quad (13)$$

where

$$K_{11}^\omega = \frac{(2\pi/L) Ra \hat{T}}{f_0 T_{0\gamma}},$$

$$K_{12}^\omega = \frac{\hat{T} (\partial f / \partial y)_0}{2(2\pi/L) T_{0\gamma}},$$

$$\begin{aligned} P_{11}^\omega = & [2k + 6\alpha k(k+1) + 6\alpha^2 k^2(k+2)] p \left[1 - \left(\frac{p}{1000} \right)^{q-1} \right] \\ & - [2 + 6\alpha k + 6\alpha^2 k(k+1)] p \ln \frac{1000}{p} \\ & + (3\alpha + 3\alpha^2 k) p \left(\ln \frac{1000}{p} \right)^2 - \alpha^2 p \left(\ln \frac{1000}{p} \right)^3, \\ P_{12}^\omega = & (\alpha k + 1) p \left[1 - \left(\frac{p}{1000} \right)^{q-1} \right] - \alpha p \ln \frac{1000}{p}, \end{aligned}$$

$$k = \frac{f_0 \eta_0}{2(2\pi/L)^2 R T_{0\gamma}},$$

and

$$q - 1 = \frac{1}{2} (1 + 4/k)^{1/2} - \frac{1}{2}.$$

Proceeding similarly with eq (11b) and (11c), we have

$$\omega_2 = \hat{\omega}_2(p) \sin \frac{2\pi}{L} (x + \lambda) \cos \frac{2\pi}{L} y$$

and

$$\omega_3 = \hat{\omega}_3(p) \sin \frac{4\pi}{L} y.$$

The solutions for $\hat{\omega}_2$ and $\hat{\omega}_3$, subject to the boundary conditions that each should vanish at the bottom and at the top of the atmosphere, are

$$\hat{\omega}_2 = K_{21}^\omega P_{21}^\omega \quad (14)$$

where

$$K_{21}^\omega = \frac{2(2\pi/L) a \hat{\phi}_{10}}{f_0 T_{0\gamma}}$$

and

$$P_{21}^\omega = (\alpha k + 1) p \left[1 - \left(\frac{p}{1000} \right)^{q-1} \right] - \alpha p \ln \frac{1000}{p}$$

and

$$\hat{\omega}_3 = K_{31}^\omega P_{31}^\omega \quad (15)$$

where

$$K_{31}^\omega = \frac{(2\pi/L)^2 \hat{\phi}_{10} \hat{T} \sin(2\pi\lambda/L)}{2f_0 T_{0\gamma}},$$

$$P_{31}^\omega = \alpha p \ln \frac{1000}{p} - \left(\alpha \frac{k}{2} + 1 \right) p \left[1 - \left(\frac{p}{1000} \right)^{q-1} \right],$$

and

$$r - 1 = \frac{1}{2} (1 + 8/k)^{1/2} - \frac{1}{2}.$$

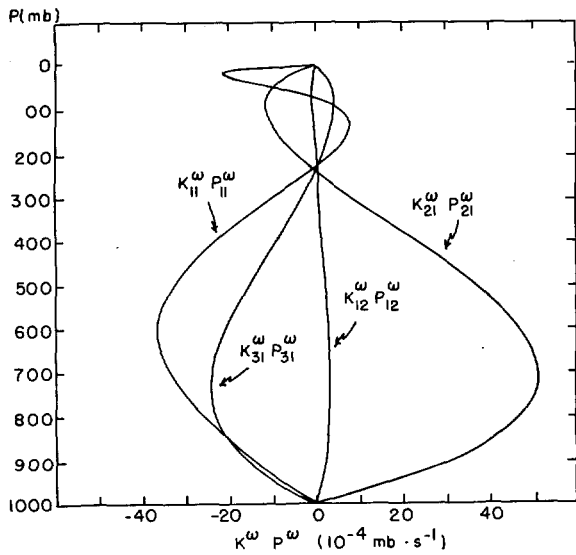


FIGURE 5.—Case C profiles of various contributions to vertical motion. The values of the parameters are $\gamma=0.114$, $f_0=\eta_0=0.92 \times 10^{-4} \text{ s}^{-1}$, and $T_0=250^\circ\text{K}$.

Each component of the vertical motion, as measured by the product of a $K^\omega P^\omega$ and the appropriate function of x and y , can be physically identified with the same process as was the corresponding part of the forcing function. Thus, for example, $K_{31}^\omega P_{31}^\omega \sin(4\pi/L)y$ is the vertical motion induced by the advection of the perturbation part of the temperature field.

Profiles of the $(K^\omega P^\omega)$'s for our sample case appear in figure 5. Note that $K_{12}^\omega P_{12}^\omega$ opposes $K_{11}^\omega P_{11}^\omega$ and is much smaller. In the troposphere, ω_1 contributes ascent from the cold trough to the downstream warm ridge. The largest component in this case is ω_2 , as shown by the profile of $K_{21}^\omega P_{21}^\omega$. It contributes ascent from the 1000-mb Low eastward to the 1000-mb High. The profile of $K_{31}^\omega P_{31}^\omega$ shows that the remaining component, ω_3 , which constitutes a meridional circulation, gives ascent to the north of the latitude of the perturbation centers and descent to the south under normal circumstances when the 1000-mb Low lies between the cold trough and the downstream warm ridge. Note that this component vanishes when $\lambda=0$ or $L/2$ (i.e., when the 1000-mb geopotential centers coincide with the temperature perturbation centers). The profiles themselves show maxima in the vicinity of 600 or 700 mb, with a reversal near the 250-mb tropopause level. The largest divergence in the low troposphere is associated with ω_2 .

Patterns for case C at 800 and at 400 mb are shown in figure 6, while a vertical cross section along $y=0$ appears in figure 7. The patterns of vertical motion slope westward with elevation in the troposphere, but not as strongly as the geopotential troughs and ridges. Note that the trough line below about 750 mb lies in a region of ascent; above this level, descent occurs in the trough up to the tropopause. At all levels, however, $\partial\omega/\partial p$ is positive at the

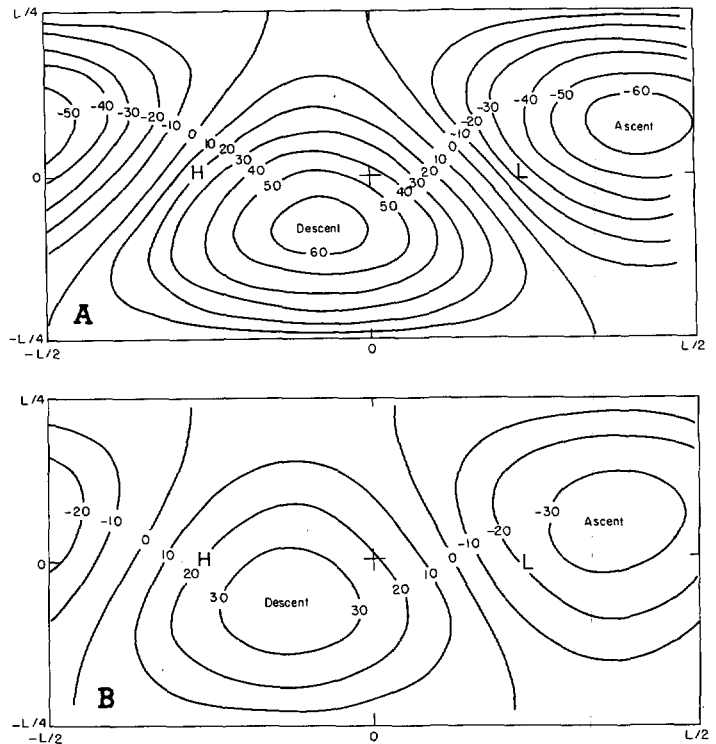


FIGURE 6.—Vertical motion for case C at (A) 800 mb and (B) 400 mb. The isopleths are labeled in units of $10^{-4} \text{ mb}\cdot\text{s}^{-1}$. The positions of the 1000-mb Lows and Highs are indicated by letters.

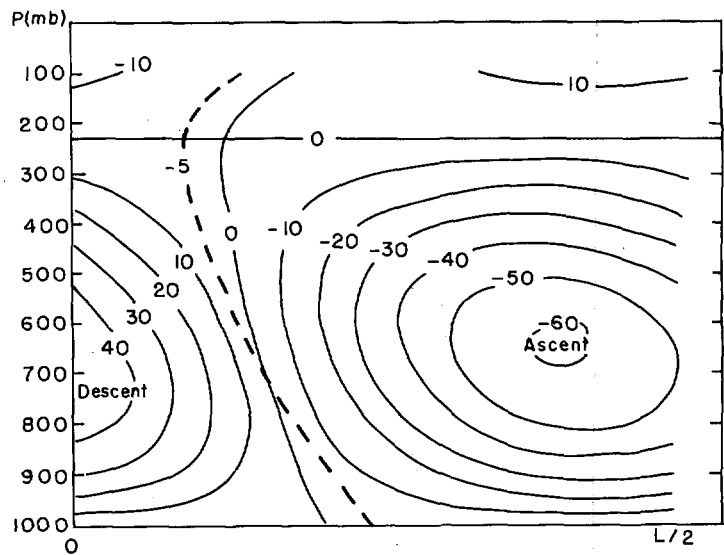


FIGURE 7.—Case C vertical cross section of vertical motion along $y=0$. The isopleths are labeled in units of $10^{-4} \text{ mb}\cdot\text{s}^{-1}$. The position of the geopotential trough is shown as a dashed line.

trough, implying that horizontal convergence is leading to intensification.

The patterns of vertical motion, though of course not amenable to verification by direct observation, seem to be consistent with our generally accepted notions with respect to both magnitude and distribution. Above the tropopause, our results are not to be trusted since the

forcing functions become unrealistically intense and are too highly correlated with tropospheric patterns. The tropospheric maxima occur at a somewhat lower elevation than one might expect. This elevation in the model, though subject to some variation with wavelength and static stability, is determined principally by the choice of tropopause level (which tends to act as an upper lid) and by the variation of the temperature field with pressure. The low maximum is associated with the rapid upward decrease of magnitude of the temperature gradient, which as discussed above may be unrealistic in some instances. The magnitude of the vertical motion is doubtless insufficient to account for heavy rainstorms of either large or small scale; but latent heat release, which plays a most important role in these situations, is absent in the model.

4. FIELD OF GEOPOTENTIAL TENDENCY

Once the field of vertical motion has been obtained, the most straightforward way of obtaining the geopotential tendencies is to solve the vorticity eq (3). The vorticity advection is evaluated from eq (8) and $\partial\omega/\partial p$ by differentiating the solution (10). Then eq (3) becomes, schematically,

$$\nabla^2\chi(x, y, p) = F_1(p) \sin \frac{2\pi}{L} x \cos \frac{2\pi}{L} y + F_2(p) \sin \frac{2\pi}{L} (x+\lambda) \times \cos \frac{2\pi}{L} y + F_3(p) \sin \frac{4\pi}{L} y \quad (16)$$

where $\chi = \partial\phi/\partial t$.

As with the omega equation, we will undertake a piecemeal solution. That is, let

$$\chi = \chi_1 + \chi_2 + \chi_3 \quad (17)$$

where

$$\nabla^2\chi_1 = F_1(p) \sin \frac{2\pi}{L} x \cos \frac{2\pi}{L} y$$

$$\nabla^2\chi_2 = F_2(p) \sin \frac{2\pi}{L} (x+\lambda) \cos \frac{2\pi}{L} y,$$

and

$$\nabla^2\chi_3 = F_3(p) \sin \frac{4\pi}{L} y.$$

Assuming that each component of χ vanishes where the corresponding forcing function vanishes in the horizontal, we have

$$\chi_1 = \hat{\chi}_1 \sin \frac{2\pi}{L} x \cos \frac{2\pi}{L} y$$

where

$$\hat{\chi}_1 = -F_1(p)/2(2\pi/L)^2.$$

Similarly,

$$\chi_2 = \hat{\chi}_2 \sin \frac{2\pi}{L} (x+\lambda) \cos \frac{2\pi}{L} y,$$

and

$$\chi_3 = \hat{\chi}_3 \sin \frac{4\pi}{L} y.$$

When the $F(p)$'s are evaluated, we find

$$\hat{\chi}_1 = K_{11}^x P_{11}^x - K_{12}^x P_{12}^x + K_{13}^x P_{13}^x - K_{14}^x P_{14}^x \quad (18)$$

where

$$K_{11}^x = \frac{R\hat{T}(\partial f/\partial y)_0}{2(2\pi/L)};$$

$$P_{11}^x = \left(\ln \frac{1000}{p}\right) \left(1 - \frac{\alpha}{2} \ln \frac{1000}{p}\right);$$

$$K_{12}^x = \frac{(2\pi/L)R^2\alpha\hat{T}}{f_0};$$

$$P_{12}^x = \left[\left(\ln \frac{1000}{p}\right) \left(1 - \frac{\alpha}{2} \ln \frac{1000}{p}\right)\right]^2;$$

$$K_{13}^x = \frac{\eta_0 R \alpha \hat{T}}{2(2\pi/L)T_{0\gamma}};$$

$$P_{13}^x = [2k + 6\alpha k(k+1) + 6\alpha^2 k^2(k+2)] \left[q \left(\frac{p}{1000}\right)^{q-1} - 1 \right] - [2 + 6\alpha k + 6\alpha^2 k(k+1)] \left(1 - \ln \frac{1000}{p}\right) + (3\alpha + 3\alpha^2 k) \left[2 \ln \frac{1000}{p} - \left(\ln \frac{1000}{p}\right)^2 \right] - \alpha^2 \left[3 \left(\ln \frac{1000}{p}\right)^2 - \left(\ln \frac{1000}{p}\right)^3 \right];$$

$$K_{14}^x = \frac{f_0 \eta_0 \hat{T}(\partial f/\partial y)_0}{4(2\pi/L)^2 T_{0\gamma}};$$

$$P_{14}^x = \alpha \left(1 - \ln \frac{1000}{p}\right) - (\alpha k + 1) \left[q \left(\frac{p}{1000}\right)^{q-1} - 1 \right].$$

Similarly,

$$\hat{\chi}_2 = K_{21}^x P_{21}^x - K_{22}^x + K_{23}^x P_{23}^x \quad (19)$$

where

$$K_{21}^x = \frac{(2\pi/L)R\alpha\hat{\phi}_{10}}{f_0};$$

$$P_{21}^x = \left(\ln \frac{1000}{p}\right) \left(1 - \frac{\alpha}{2} \ln \frac{1000}{p}\right);$$

$$K_{22}^x = \frac{\hat{\phi}_{10}(\partial f/\partial y)_0}{2(2\pi/L)};$$

$$K_{23}^x = \frac{\eta_0 \alpha \hat{\phi}_{10}}{(2\pi/L)T_{0\gamma}};$$

$$P_{23}^x = (\alpha k + 1) \left[q \left(\frac{p}{1000}\right)^{q-1} - 1 \right] - \alpha \left(1 - \ln \frac{1000}{p}\right).$$

Finally,

$$\hat{\chi}_3 = K_{31}^x P_{31}^x \quad (20)$$

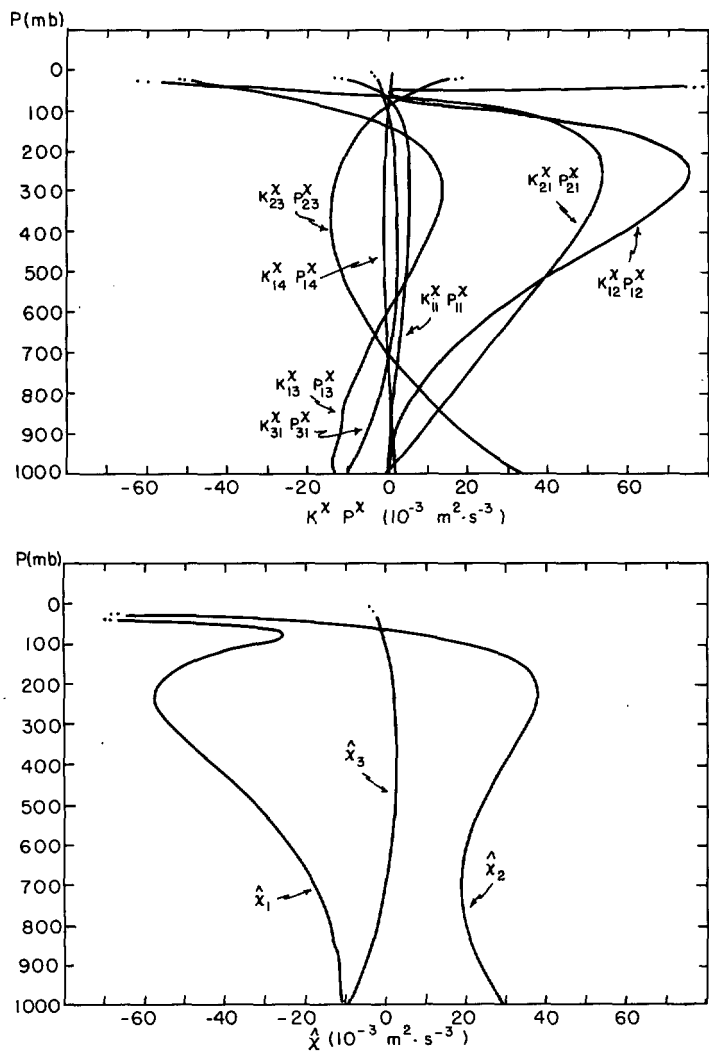


FIGURE 8.—Case C profiles of various contributions to geopotential tendency.

where

$$K_{31}^X = \frac{\eta_0 \phi_{10} \hat{T} \sin(2\pi\lambda/L)}{8T_0\gamma};$$

$$P_{31}^X = \alpha \left(1 - \ln \frac{1000}{p}\right) - \left(\alpha \frac{k}{2} - 1\right) \left[r \left(\frac{p}{1000}\right)^{r-1} - 1 \right].$$

Again, we can trace out the physical identity of the various parts of the geopotential tendency. Thus, for example, $K_{11}^X P_{11}^X$, $K_{12}^X P_{12}^X$, $K_{21}^X P_{21}^X$, and K_{22}^X represent the effects of vorticity advection, while the remaining terms represent effects of horizontal divergence. The reader can work out the identity of each term further by examining the structure of the (K^X)'s.

Profiles of the ($K^X P^X$)'s and of the $\hat{\chi}$'s appear in figure 8. Near 1000 mb, we see that divergence effects dominate; and in this case, the one attributable to the interaction of the 1000-mb flow and the meridional temperature gradient is by far the most important. Between 700 and 600 mb, divergence effects are at a minimum (though there is no single level of nondivergence in the model), accounting

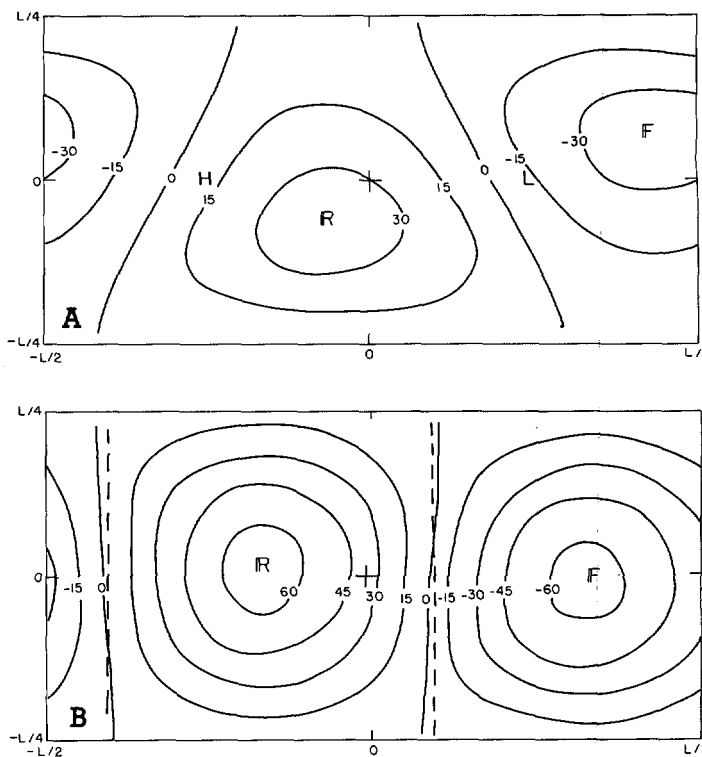


FIGURE 9.—Case C geopotential tendency at (A) 1000 mb and (B) 300 mb. The isopleths are labeled in units of $10^{-3} \text{ m}^2 \text{ s}^{-3}$. The positions of the trough and ridge at 300 mb are indicated by dashed lines. The positions of the 1000-mb Low and High are shown by letters.

for the moderate success of mid-tropospheric barotropic prediction even when applied to highly baroclinic situations. In the upper troposphere, vorticity advection dominates, but divergence exerts a strong modifying influence.

Patterns of geopotential tendency at 1000 and at 300 mb are illustrated in figure 9. In synoptically more familiar terms, the maximum at the former level corresponds to a change in sea-level pressure of about 5.2 mb/3 hr and at the latter level to a 12-hr change of height of 280 m, both quite reasonable. Qualitatively, it appears from a comparison of figure 9 with figures 3 and 4 that the 1000-mb Low is deepening and moving east-northeastward and that the High is building and moving east-southeastward, while the trough and ridge at 300 mb are moving eastward and amplifying.

5. MOTION OF GEOPOTENTIAL FEATURES

Petterssen's (1956, pp. 48-49) formulas can be used to evaluate exactly the motion and intensification of features of the geopotential field. Consider, for example, the trough at $y=0$. For the eastward speed of this feature, we may write

$$c_x(p) = -\frac{\partial x / \partial x}{\partial^2 \phi / \partial x^2}(x_T, 0, p) \tag{21}$$

where $x = x_T$ is the position of the trough axis. For finding x_T , we differentiate eq (8) with respect to x , set the result

equal to zero, and look for a solution between $x=0$ and $x=L/2-\lambda$. Thus, we find

$$\frac{2\pi}{L} x_T(p) = \tan^{-1} \left[\frac{\hat{\phi}_{10} \sin (2\pi\lambda/L)}{R\hat{T} \left(\ln \frac{1000}{p} \right) \left(1 - \frac{\alpha}{2} \ln \frac{1000}{p} \right) - \hat{\phi}_{10} \cos (2\pi\lambda/L)} \right] \tag{22}$$

The appropriate expression for $c_x(p)$ is found by differentiating eq (17) once and eq (8) twice with respect to x , leading to

$$c_x(p) = \frac{\hat{\chi}_1(p) \cos (2\pi x_T/L) + \hat{\chi}_2(p) \cos [2\pi(x_T + \lambda)/L]}{(2\pi/L) \left\{ \hat{\phi}_{10} \cos [2\pi(x_T + \lambda)/L] - R\hat{T} \left(\ln \frac{1000}{p} \right) \left(1 - \frac{\alpha}{2} \ln \frac{1000}{p} \right) \cos (2\pi x_T/L) \right\}} \tag{23}$$

Results for our sample case are given in table 1. For comparison, the observed 12-hr displacements at 1000 and at 500 mb were at rates of 11 m/s and 12 m/s, respectively, in reasonably good agreement with the theoretical values. The first prominently unrealistic result of our calculations is the relatively slow trough speed in the lower troposphere above 1000 mb. The real atmosphere avoids the development of intermediate-level trough lag by means which are evidently not contained in our theory.

The northward speed of the 1000-mb Low is given by

$$c_y(1000) = -\frac{\partial x/\partial y}{\partial^2 x/\partial y^2} \left(\frac{L}{2} - \lambda, 0, 1000 \right) \tag{24}$$

Proceeding as with eq (21), we find that

$$c_y(1000) = \frac{\eta_0 \hat{T} \sin (2\pi\lambda/L) \left[(r-1) \left(\alpha \frac{k}{2} + 1 \right) - \alpha \right]}{4(2\pi/L) T_0 \gamma} \tag{25}$$

For case C, the computed value of $c_y(1000)$ is 9.1 m/s, while the observed 12-hr displacement rate of the surface Low is 7.5 m/s.

At 1000 mb, the eastward speed of the Low as given by eq (23) can be expressed in terms of the basic param-

eters of the model as

$$c_x(1000) = c_{x1} \cos (2\pi\lambda/L) + c_{x2} \tag{26}$$

where

$$c_{x1} = \frac{\eta_0 \hat{T}}{2(2\pi/L)^2 T_0 \gamma \hat{\phi}_{10}} \left(Ra \{ [2k + 6\alpha k(k+1) + 6\alpha^2 k^2(k+2)](q-1) - [2 + 6\alpha k + 6\alpha^2 k(k+1)] \} + \frac{f_0(\partial f/\partial y)_0}{2(2\pi/L)^2} [(\alpha k + 1)(q-1) - \alpha] \right)$$

and

$$c_{x2} = \frac{\eta_0 a}{(2\pi/L)^2 T_0 \gamma} [(\alpha k + 1)(q-1) - \alpha] - \frac{(\partial f/\partial y)_0}{2(2\pi/L)^2}$$

represents the effects of χ_1 and χ_2 , respectively. Ordinarily, c_{x1} is distinctly smaller than c_{x2} . For example, in the sample case where c_{x2} is 13.7 m/s, c_{x1} is 4.7 m/s. Of course, in this case (since $\lambda=L/4$) it has no effect. With $\lambda=0$ (warm Lows, cold Highs), c_{x1} would retard eastward speed of the geopotential centers, while with $\lambda=L/2$ (cold Lows, warm Highs) it would have an enhancing effect. This result seems opposed to observational experience that warm Lows tend to move more rapidly than cold ones; but no extensive test of eq (26) has been performed, and the difference in observed behavior of warm and cold systems may be due to other factors, principally differences in the meridional temperature gradient.

The response of c_{x2} to variation of parameters of the model is illustrated in figure 10. Isopleths are shown for three values of the "vorticity stability" factor, $\eta_0/T_0\gamma$. The intermediate value corresponds to intermediate atmospheric values, say,

$$\eta_0 = 10^{-4} s^{-1}, T_0 = 250^\circ K, \gamma = 0.144,$$

TABLE 1.—Case C eastward speed of trough

Pressure (mb)	x_T (% of L)	c_x (m/s)
100	14	13.5
200	10	18.1
300	10	17.1
400	11	14.9
500	12	12.7
600	14	10.9
700	16	9.9
800	19	10.0
900	22	11.4
1000	25	13.7

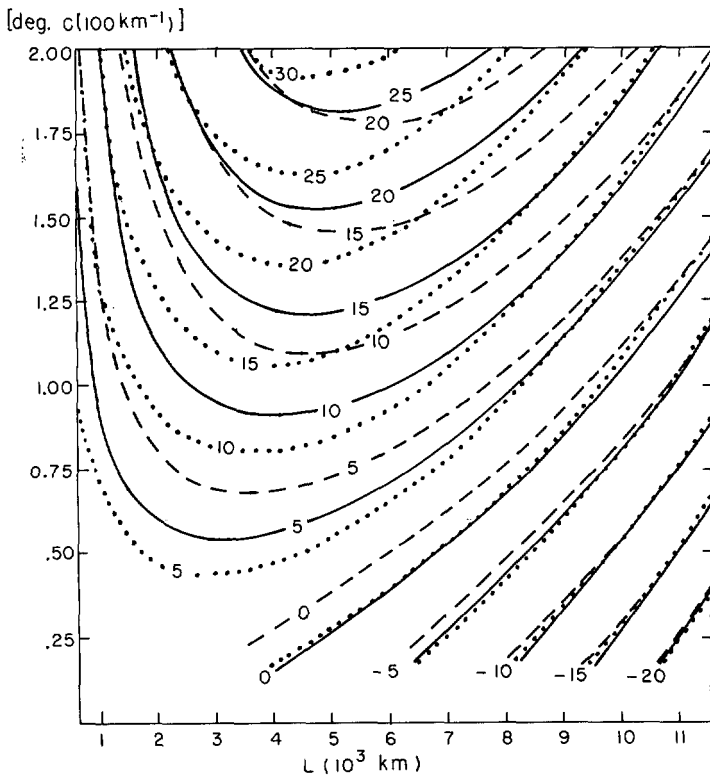


FIGURE 10.—Eastward speed c_{z2} of the 1000-mb center as a function of wavelength and meridional temperature gradient for selected values of the vorticity-stability parameter. The dashed, solid, and dotted lines are for values of 1.4 , 2.8 , and $5.6 \times 10^{-6} \text{ s}^{-1}$, respectively. The intermediate value most nearly represents average atmospheric conditions. The isotachs are labeled in meters per second.

a vertical temperature gradient halfway between isothermal conditions and the dry-adiabatic lapse rate. The smaller value might be regarded as appropriate for anticyclonic conditions (small vorticity and large stability), while the larger might be thought of as representing cyclonic conditions. Only qualitative inferences at best could be drawn from these distinctions because our theory is based on horizontal uniformity of this parameter over both the cyclonic and anticyclonic portions of the pattern. The range of wavelengths presented in figure 10 is extravagant because our β -plane geometry is inadequate for the largest, while the smallest is below the limits of size regarded as appropriate for geostrophic analysis. With these disclaimers in mind, we note in figure 10 that the zonal motion of centers is eastward unless the wavelength is too large or the meridional temperature gradient is too small. This motion has a maximum in the wavelength range from 2000 to 6000 km where our theory is most appropriate and where the values look synoptically reasonable. This maximum speed increases somewhat more than linearly with the meridional temperature gradient. As the vorticity-stability factor increases, eastward speed increases and the wavelength of maximum speed decreases through most of the region of interest.

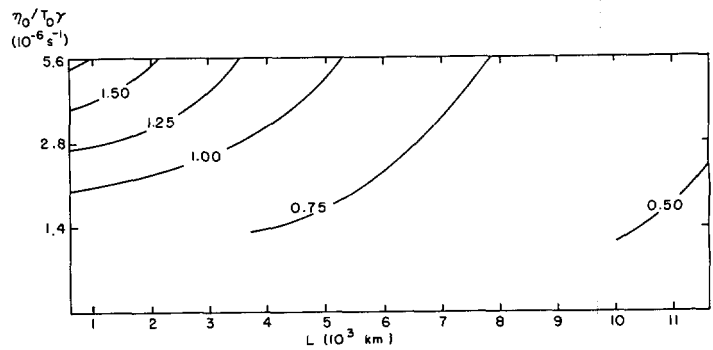


FIGURE 11.—Northward speed c_{y3} of the 1000-mb center as a function of wavelength and vorticity-stability parameter for $\hat{T}=1$. The isotachs are labeled in meters per second.

We can examine the meridional motion of centers by writing

$$c_y(1000) = c_{y3} \sin(2\pi\lambda/L) \tag{27}$$

where

$$c_{y3} = \frac{\eta_0 \hat{T} \left[(r-1) \left(\alpha \frac{k}{2} + 1 \right) - \alpha \right]}{4(2\pi/L) T_0 \gamma}$$

Note that this motion is always northward for centers (usually cyclonic) between the cold trough and the downstream warm ridge, southward for centers (usually anticyclonic) between this trough and the upstream ridge. This finding is consistent with Petterssen's (1956) evidence for the systematic meridional motion of surface cyclones and anticyclones, but suggests that our model, with centers at a common latitude, can have only a transitory close resemblance to real life.

The behavior of c_{y3} in our model is illustrated in figure 11 for a nominal value of $\hat{T}=1$. Note that the value of c_{y3} is directly proportional to the magnitude of the temperature perturbation. For a given value of \hat{T} , we see from figure 11 that c_{y3} increases with decreasing wavelength and with increasing value of the vorticity-stability parameter and that the values are synoptically realistic.

It is interesting to examine the steering concept in the context of our theory. By "steering" we mean the time-honored belief that the motion of a surface cyclone or anticyclone is controlled by the flow aloft over the surface center. We have shown here that the motion of 1000-mb centers is due to divergence at this level rather than to transport of some quantity by the flow at upper levels. The divergence producing zonal motion is associated primarily with that part of ω due to the meridional temperature gradient, while the meridional motion is attributable to the temperature perturbation; but the structure of the relationships is different. Thus, the relationship between the displacement velocity of the center and the overlying wind velocity is far from obvious.

For orientation, consider the flow at 500 mb for the case of $\lambda = L/4$. Over the 1000-mb center, its components are

$$\left. \begin{aligned} u_5 &= -(1/f_0)\partial\phi/\partial y \\ v_5 &= (1/f_0)\partial\phi/\partial x \end{aligned} \right\} \left(\frac{L}{2} - \lambda, 0, 500 \right).$$

From eq (8), we find for this case that

$$u_5 = \frac{Ra}{f_0} \left[\ln 2 - \frac{\alpha}{2} (\ln 2)^2 \right]$$

and

$$v_5 = \frac{(2\pi/L)R\hat{T}}{f_0} \left[\ln 2 - \frac{\alpha}{2} (\ln 2)^2 \right].$$

For case C we have $u_5 = 18.1$ m/s and $v_5 = 25.4$ m/s, while c_{z2} and c_{v3} are 13.7 and 9.1 m/s, respectively, so that the 1000-mb Low is moving to the right of the 500-mb flow. Specifically, the former is toward 056° at 16.0 m/s while the latter is toward 035° at 31.2 m/s.

The properties of the model are examined with respect to steering in figure 12. Note that the ratio, c_{z2}/u_5 , displays a maximum at a wavelength between 2000 and 6000 km, depending on the vorticity-stability parameter and the meridional temperature gradient. The ratio for a given wavelength varies directly with these two parameters and can achieve values greater than unity. The ratio c_{v3}/v_5 (which is independent of \hat{T}) is more modest, increasing with wavelength and with the vorticity-stability parameter. For the case of $\lambda = L/4$, the Low moves to the right of the 500-mb flow when $c_{z2}/u_5 > c_{v3}/v_5$. Observe in figure 12 that this condition prevails for conditions under which most cyclones are observed. (The amount of deviation depends additionally on \hat{T} and is not easily portrayed.) As λ approaches zero or $L/2$, both the motion and the 500-mb wind approach a west-to-east direction.

These results provide an explanation for Austin's (1947) empirical findings that surface cyclones move to the right of the upper flow and that there is little correlation between cyclone speed and speed of the flow aloft.

Of course, our theory is symmetric: we find also that 1000-mb anticyclones move to the left of the upper flow, but we are not aware of any empirical studies that might be used as a test of this result.

6. INTENSIFICATION OF GEOPOTENTIAL FEATURES

The deepening of Lows and the building of Highs is as important as their motion and can be readily examined with our model. Consider the 1000-mb Low. The deepening rate is given by the geopotential tendency at the center, which from eq (17) can be expressed as

$$x \left(\frac{L}{2} - \lambda, 0, 1000 \right) = \hat{\chi}_1(1000) \sin(2\pi\lambda/L). \quad (28)$$

We see immediately that deepening, if occurring at all, will be a maximum when $\lambda = L/4$ (i.e., when the cold trough lies to the west and the warm ridge to the east of the surface center, a synoptically familiar necessity for cyclogenesis). No deepening occurs when the 1000-mb

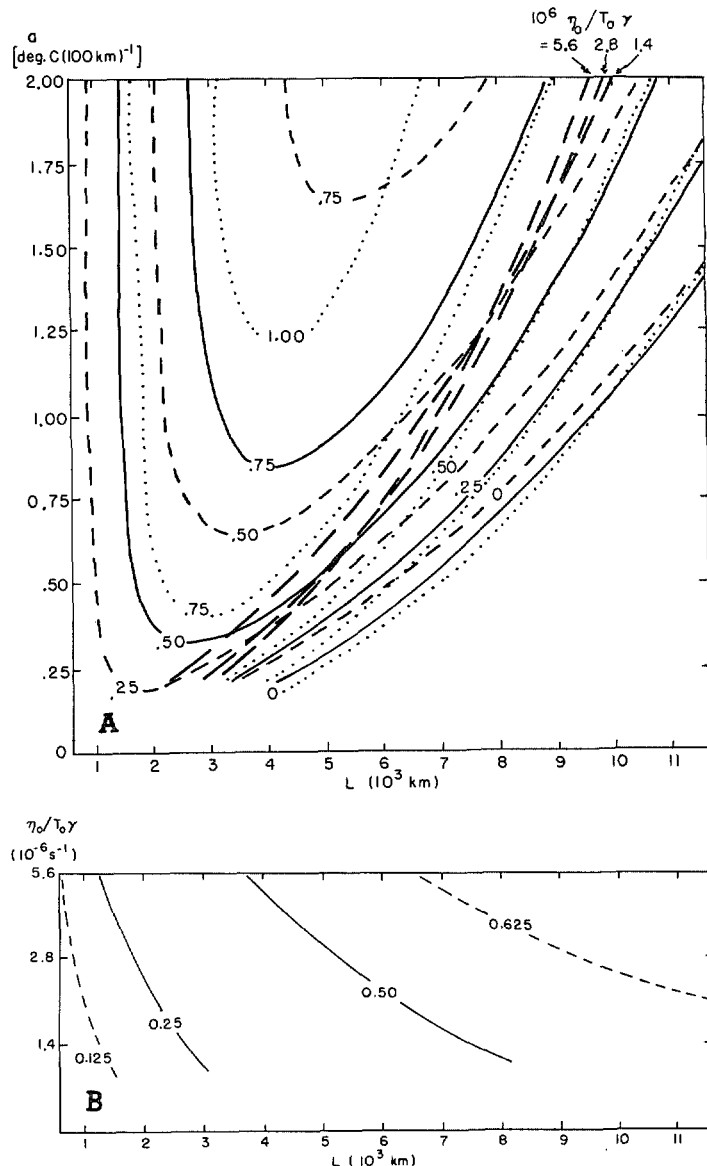


FIGURE 12.—Ratio of (A) c_{z2} to the zonal component of a 500-mb wind as a function of wavelength and meridional temperature gradient and (B) c_{v3} to the meridional component of a 500-mb wind as a function of wavelength and vorticity-stability parameter. No isopleths are shown where the ratios are negative. In (A), the dashed, solid, and dotted lines are as explained in figure 10. The heavy dashed lines are loci of maximum wavelength for which the 1000-mb Low moves to the right of the upper level flow.

Low coincides with either the warm ridge or the cold trough; the latter presumably representing the classical occluded cyclone stage.

From eq (18) we find, since $P_{11}^x = P_{12}^x = 0$, that

$$\begin{aligned} \hat{\chi}_1(1000) &= \frac{\eta_0 Ra \hat{T}}{2(2\pi/L)T_{0\gamma}} \{ [2k + 6\alpha k(k+1) + 6\alpha^2 k^2(k+2)](q-1) \\ &\quad - [2 + 6\alpha k + 6\alpha^2 k(k+1)] \} + \frac{f_0 \eta_0 \hat{T} (\partial f / \partial y)_0}{4(2\pi/L)^3 T_{0\gamma}} \\ &\quad \times [(\alpha k + 1)(q-1) - \alpha]. \quad (29) \end{aligned}$$

For our sample case, in which $\lambda = L/4$, the value of

$\hat{\chi}_1(1000)$ is $-109 \times 10^{-4} \text{ m}^2/\text{s}^3$, which corresponds to a deepening rate for sea-level pressure of about $-6.4 \text{ mb}(12 \text{ hr})^{-1}$, while the observed 12-hr deepening was -8 mb . The agreement is not as good as it appears, however, for we have taken no theoretical account of the filling effect of surface friction, which we shall see is far from negligible.

Despite the complex structure of eq (29), we can draw some inferences from it. Both terms on the right side represent effects of divergence associated with ω_1 , the component of vertical motion arising from the temperature field alone. This vertical motion, as discussed above, is due to vorticity advection. The first term on the right side of eq (29) is associated with advection of relative vorticity, while the second is associated with advection of earth vorticity, as indicated by the presence of $(\partial f/\partial y)_0$ in its coefficient. Qualitatively, the first produces upward motion, and 1000-mb convergence, east of the cold perturbation, while the second produces a counteracting descent with divergence at 1000 mb. Since the 1000-mb Low ordinarily lies between the cold trough and the downstream warm ridge, the first term represents the active deepening mechanism, while the second acts as a brake. This finding is entirely consistent with Petterssen's (1956, p. 337) view of the conditions for cyclone development.

Further examination of eq (29) suggests because of the exponent of L that the braking action of the second term will increase with increasing wavelength more rapidly than the deepening action of the first term, so that there will be a limiting wavelength above which no net intensification will occur. This finding is tentative for the moment because k and q are also functions of wavelength. The occurrence of intensification is also controlled by the meridional temperature gradient, since for any wavelength there is a minimum required value of a for net deepening.

The temperature perturbation \hat{T} and the vorticity-stability parameter $\eta_0/T_0\gamma$ have no effect on the occurrence or nonoccurrence of deepening but are directly proportional to its magnitude.

These findings are confirmed and made quantitative in figure 13. If we regard $\hat{\chi}_1$ as a measure of the instability of the baroclinic system, we see that there is a wavelength of maximum instability in the region from 1500 to 3500 km, which increases with the meridional temperature gradient and with the value of the vorticity-stability parameter. The anticipated longwave cutoff is clearly indicated, but there appears to be no limiting short wavelength for intensification.

The preferred sizes of observed cyclones and anti-cyclones should and do correspond to the wavelengths of maximum instability. We are unaware of observational evidence to confirm the computed relationship between preferred wavelength and meridional temperature gradient. We can argue, however, that the relationship between the preferred wavelength and the vorticity-stability parameter is supported by observational experience that Highs are larger than Lows and that small hydrostatic stability tends to favor small synoptic scale disturbances.

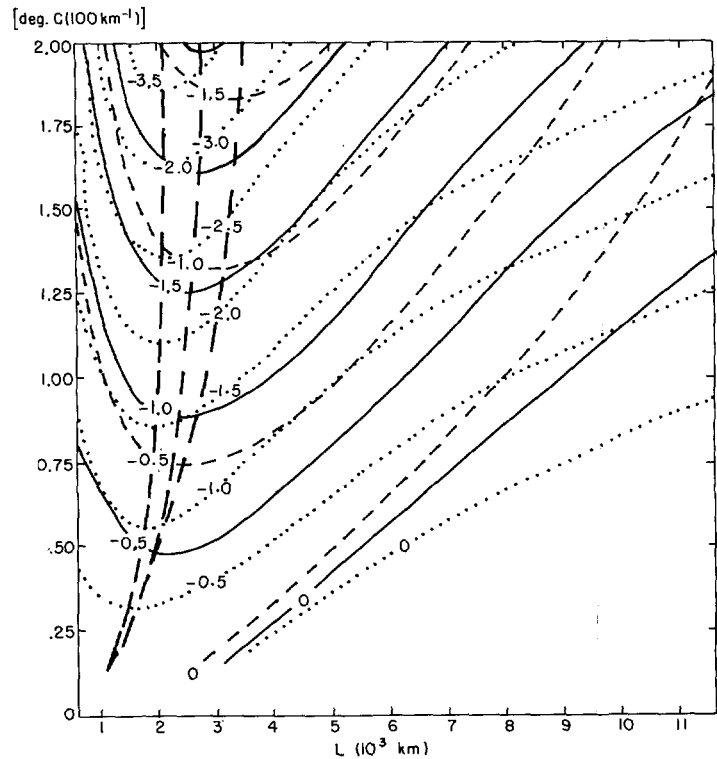


FIGURE 13.—Deepening rate $\hat{\chi}_1$ of the 1000-mb cyclone as a function of wavelength and meridional temperature gradient for selected values of the vorticity-stability parameter and for $\hat{T}=1^\circ\text{C}$. The isopleths are labeled in units of $10^{-3} \text{ m}^2\text{-s}^{-3}$. The dashed, solid, and dotted lines are as explained in figure 10. The dashed lines are loci of the wavelength of maximum deepening rate.

As mentioned above, we have overestimated the theoretical deepening rates because of neglect of surface friction. Let us now suppose, somewhat artificially, that the 1000-mb surface lies at the top of the surface friction layer. Frictional divergence or convergence within the layer produces a vertical motion at the top which we will regard as a lower boundary value ω_{10} .

For evaluating this effect, we start with Petterssen's (1956, p. 83) calculation that, with an angle of 25° between the surface isobars and the wind at anemometer level, the mass transport across the isobars within the friction layer is 14 percent of the geostrophic transport along the isobars. Neglecting vertical variations of density and of geostrophic wind in a friction layer of depth h , we can express this result as

$$\int_0^h \mathbf{V}_n dz = 0.14 h \mathbf{k} \times \mathbf{V}_g$$

where \mathbf{V}_n is the wind component normal to the geostrophic wind, \mathbf{V}_g . If variations of f are neglected (so that $\nabla \cdot \mathbf{V}_g = 0$) as well as horizontal variations of density and h , then the equation of continuity yields

$$\omega_h = -\nabla \cdot \int_0^h \mathbf{V}_n dz = -0.14 h \nabla \cdot \mathbf{k} \times \mathbf{V}_g = 0.14 h \zeta_{10}$$

Since $\omega_{10} = -g\rho_{10}\omega_h$, and with an assumed friction layer

depth of 1 km, we find approximately that

$$\omega_{10} = -14 \zeta_{10} \text{ mb/s.} \quad (30)$$

In the light of eq (7) and since $\zeta_{10} = \nabla^2 \phi_{10} / f_0$, we have

$$\omega_{10} = \hat{\omega}_{10} \cos \frac{2\pi}{L} (x + \lambda) \cos \frac{2\pi}{L} y \quad (31)$$

where

$$\hat{\omega}_{10} = \frac{28(2\pi/L)^2 \hat{\phi}_0}{f_0}$$

This result yields a frictional updraft over the surface cyclone and a downdraft over the anticyclone.

For obtaining the distribution of this vertical motion above the 1000-mb level, we may simply define an additional component of vertical motion, ω_4 , which satisfies

$$\left(\nabla^2 + \frac{f_0 \eta_0 p^2}{RT_0 \gamma} \frac{\partial^2}{\partial p^2} \right) \omega_4 = 0 \quad (32)$$

subject to boundary conditions that $\omega_4(0) = 0$ and $\omega_4(1000) = \omega_{10}$. We shall assume that ω_4 is distributed horizontally as ω_{10} , so that

$$\nabla^2 \omega_4 = -2(2\pi/L)^2 \omega_4.$$

The solution of eq (32) is then

$$\omega_4 = \hat{\omega}_{10} \left(\frac{p}{1000} \right)^{\alpha-1} \cos \frac{2\pi}{L} (x + \lambda) \cos \frac{2\pi}{L} y. \quad (33)$$

Since the exponent in eq (33) is positive, this frictional vertical motion decreases with elevation, so that we find divergence over the surface cyclone and convergence over the surface anticyclone, tending in both instances to weaken the circulation features.

For obtaining the quantitative effect, we add χ_4 , a frictional contribution, to the geopotential tendency eq (17). This contribution satisfies

$$\nabla^2 \chi_4 = f_0 \eta_0 \frac{\partial \omega_4}{\partial p}$$

If we assume that the horizontal distribution of χ_4 matches that of ω_4 and use eq (33) and (31), we arrive at

$$\chi_4 = \hat{\chi}_4 \cos \frac{2\pi}{L} (x + \lambda) \cos \frac{2\pi}{L} y \quad (34)$$

where

$$\hat{\chi}_4 = \frac{7f_0 \hat{\phi}_{10} \left(1 + \frac{8(2\pi/L)^2 RT_0 \gamma}{f_0 \eta_0} \right)^{1/2}}{1000} \left(\frac{p}{1000} \right)^{\alpha-1}.$$

At the 1000-mb level in our sample case, $\hat{\chi}_4 = 40 \times 10^{-4} \text{ m} \cdot \text{s}^{-2}$, corresponding to filling of the central sea-level pressure at the rate of about 2.3 mb (12 hr) $^{-1}$. From our previous calculation of the frictionless deepening rate, we see that the net rate with the frictional effect included is $-4.1 \text{ mb (12 hr)}^{-1}$, only about half of the observed rate.

It is clear from the definition of $\hat{\chi}_4$ that, for given values of the other parameters, the frictional filling rate increases as the wavelength decreases. Since we have seen that the frictionless deepening rate decreases with decreasing wavelength when the length is sufficiently small, the frictional mechanism provides a shortwave cutoff for intensification provided the disturbance is of finite amplitude (i.e., $\hat{\phi}_{10} \neq 0$). It also shifts the wavelength of maximum intensification to somewhat larger values. The amount of this shift and the exact position of the shortwave cutoff depend on virtually all the parameters of the model and cannot be easily summarized.

Moreover, it is evident from a comparison of $\hat{\chi}_1$ and $\hat{\chi}_4$ that friction establishes a limiting intensity of the circulation in any event because $\hat{\chi}_1$ is independent of $\hat{\phi}_{10}$ while $\hat{\chi}_4$ is directly proportional to it. This limiting intensity for the case of $\lambda = L/4$ is

$$\hat{\phi}_{10} = \frac{1000 \hat{\chi}_1}{7f_0 \left(1 + \frac{8(2\pi/L)^2 RT_0 \gamma}{f_0 \eta_0} \right)^{1/2}}$$

which for our sample case is $2.78 \times 10^3 \text{ m}^2 \cdot \text{s}^{-2}$. This value corresponds to a range of sea-level pressure between low and high of about 74 mb, somewhat high but not hopelessly unrealistic. The discrepancy may be due in part to the linear variation of ω_{10} with ζ_{10} shown in eq (30). Perhaps, the frictional vertical motion should vary more strongly with relative vorticity. Moreover, we traditionally regard intensification as terminating with occlusion (i.e., $\lambda \rightarrow L/2$) rather than with a frictional balance, but we are not aware of any observational studies bearing on this point.

Finally, we have the impression that this model, especially with the inclusion of frictional effects, is incapable of accounting for the really explosive cyclogenetic instances that, for example, characterize the synoptic meteorology of the winter oceans. These intense storms must depend crucially on some form of diabatic heating, either sensible heat transfer from the sea or release of latent heat of condensation. The failure of current numerical prediction techniques to predict this phenomenon adequately, though due perhaps to large grid distances employed operationally, confirms our suspicions.

7. FIELD OF TEMPERATURE TENDENCY

The pattern of local rate of change of temperature will complete our picture and can be obtained in either of two ways: directly from the thermodynamic eq (2) or by differentiating the geopotential tendency eq (17). We chose the latter approach, actually to check the correctness of the work on which eq (17) depends.

From the equation of state and the hydrostatic equation,

$$\frac{\partial T}{\partial t} = -\frac{p}{R} \frac{\partial \chi}{\partial p}$$

In obtaining $\partial \chi / \partial p$ from eq (17), we differentiate the (P^*)'s and rearrange the coefficients and the resulting

pressure functions, arriving at

$$\frac{\partial T}{\partial t} = \left(\frac{\partial T}{\partial t}\right)_1 \sin \frac{2\pi}{L} x \cos \frac{2\pi}{L} y + \left(\frac{\partial T}{\partial t}\right)_2 + \sin \frac{2\pi}{L} (x+\lambda) \cos \frac{2\pi}{L} y + \left(\frac{\partial T}{\partial t}\right)_3 \sin \frac{4\pi}{L} y \quad (35)$$

where

$$\left(\frac{\partial T}{\partial t}\right)_1 = K_{11}^T P_{11}^T - K_{12}^T P_{12}^T; \quad (36)$$

$$K_{11}^T = \frac{\hat{T}(\partial f/\partial y)_0}{2(2\pi/L)};$$

$$P_{11}^T = 1 + \alpha \left(k - \ln \frac{1000}{p}\right) - (\alpha k + 1) \left(\frac{p}{1000}\right)^{q-1};$$

$$K_{12}^T = \frac{2(2\pi/L)Ra\hat{T}}{f_0};$$

$$P_{12}^T = [k + 3\alpha k(k+1) + 3\alpha^2 k^2(k+2)] \left[q \left(\frac{p}{1000}\right)^{q-1} - 1\right] - [k + 3\alpha k^2 + 3\alpha^2 k^2(k+1)] - (3\alpha k + 3\alpha^2 k^2) \left(1 - \ln \frac{1000}{p}\right) - (3/2)\alpha^2 k \left[2 \ln \frac{1000}{p} - \left(\ln \frac{1000}{p}\right)^2\right];$$

$$\left(\frac{\partial T}{\partial t}\right)_2 = K_{21}^T P_{21}^T; \quad (37)$$

$$K_{21}^T = \frac{(2\pi/L)a\hat{\phi}_{10}}{f_0};$$

$$P_{21}^T = 1 - \alpha \ln \frac{1000}{p} - 2 \left[(\alpha k + 1) \left(\frac{p}{1000}\right)^{q-1} - \alpha k\right];$$

$$\left(\frac{\partial T}{\partial t}\right)_3 = K_{31}^T P_{31}^T; \quad (38)$$

$$K_{31}^T = \frac{(2\pi/L)^3 \hat{\phi}_{10} \hat{T} \sin(2\pi\lambda/L)}{2f_0};$$

$$P_{31}^T = \left(\alpha \frac{k}{2} + 1\right) \left(\frac{p}{1000}\right)^{r-1} - \frac{\alpha k}{2}.$$

At the 1000-mb level (since $\omega_{10} = 0$), this expression should and does reduce to the expression for the temperature advection

$$\begin{aligned} \frac{\partial T_{10}}{\partial t} &= -\mathbf{V}_{10} \cdot \nabla T_{10} \\ &= \frac{(2\pi/L)^2 \hat{\phi}_{10} \hat{T} \sin(2\pi\lambda/L)}{2f_0} \sin \frac{4\pi}{L} y \\ &\quad - \frac{(2\pi/L)a\hat{\phi}_{10}}{f_0} \sin \frac{2\pi}{L} (x+\lambda) \cos \frac{2\pi}{L} y. \end{aligned}$$

Profiles of the $(K^T P^T)$'s and of the $(\partial T/\partial t)$'s for case C appear in figure 14. In $(\partial T/\partial t)_1$, produced entirely by

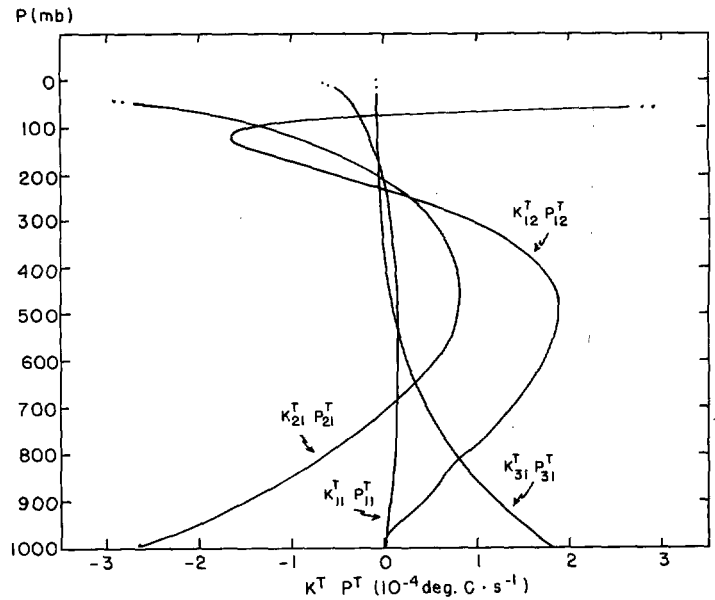


FIGURE 14.—Case C profiles of various contributions to temperature tendency.

the adiabatic heating or cooling associated with ω_1 , the contribution arising from $(\partial f/\partial y)_0$ is an order of magnitude smaller than that arising from advection of relative vorticity. This component indicates eastward progression of the cold troughs and warm ridges except at 1000 mb where the features are stationary and above the 75-mb level where the results are not to be trusted. The contribution $(\partial T/\partial t)_2$, due to advection of the zonally averaged temperature and the adiabatic effects due to ω_2 , is relatively complex. Since $\lambda = L/4$ in this case, $(\partial T/\partial t)_2$ indicates intensification of the temperature perturbations below the 700-mb level and weakening above. The final term $(\partial T/\partial t)_3$, arising from advection of the perturbed part of the temperature field and from ω_3 , yields warming north of the latitude of the perturbation centers and cooling to the south up to the 450-mb level, above which the sense reverses. At the lowest levels, $(\partial T/\partial t)_2$ and $(\partial T/\partial t)_3$ tend to dominate because of the contributions due to advection; but above 800 mb, the adiabatic heating and cooling produced by ω_1 make $(\partial T/\partial t)_1$ the largest individual term.

Patterns of temperature tendency at the 900- and 500-mb levels for our sample case are shown in figure 15. The advection-dominated pattern at the lower level is quite different from the vertical motion-dominated pattern at the higher level, but both seem synoptically reasonable, with respect to both general pattern and magnitude.

If we take the difference between the tendencies at the two levels, moreover, we find maximum destabilization occurring approximately in the path of the cyclone and stabilization ahead of the anticyclone, consistent with the characteristic observed differences in tropospheric lapse

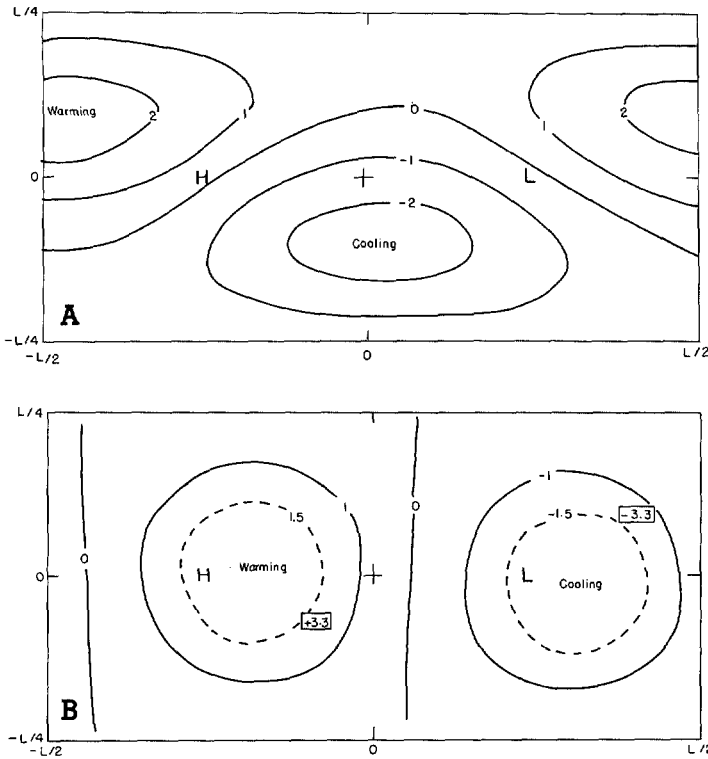


FIGURE 15.—Temperature tendency for case C at (A) 900 mb and (B) 500 mb. The isallotherms are labeled in units of $10^{-4}^{\circ}\text{C}\cdot\text{s}^{-1}$. The positions of the 1000-mb Low and High are indicated by letters. The boxed values are extrema in the difference $\partial T/\partial t$ at 500 mb— $\partial T/\partial t$ at 900 mb.

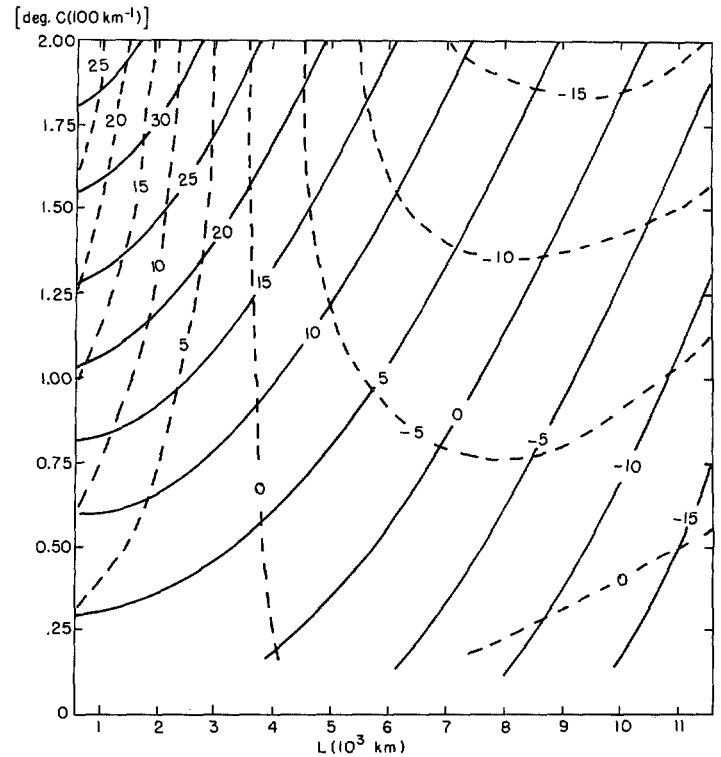


FIGURE 16.—Eastward speed of the 250-mb trough (solid), $c_x(250)$, and overtaking rate (dashed), $c_x(250) - c_x(1000)$, as a function of wavelength and meridional temperature gradient. The values of other parameters are $\eta_0/T_0\gamma = 2.8 \times 10^{-6} \text{ s}^{-1}$, $\hat{T} = 5^{\circ}\text{C}$, and $\lambda = L/4$.

rate associated with these two circulation systems. The rate, however, at the points of peak stability change is about $3.5^{\circ}\text{C}(3 \text{ hr})^{-1}$ over the layer of 400-mb depth. This value seems excessive for systems of synoptic scale and would tend after operating for a short time to cast doubt on the modeling assumption that the hydrostatic stability parameter σ is uniform on a constant-pressure surface. Thus, we find another inconsistency in the model. Evidently, the physical mechanism by which the atmosphere controls its hydrostatic stability is not entirely satisfactorily represented here.

Whether or not occlusion is occurring, or more specifically whether or not the cold trough is overtaking the 1000-mb cyclone, is a rather ambiguous question. Since the cold trough is stationary at 1000 mb in our sample case, the geopotential Low is obviously escaping from it. At higher levels, however, kinematic calculations show an appreciable rate of overtaking. Perhaps a more meaningful (but not conclusive) measurement is the eastward speed of the 250-mb trough; if it is overtaking the 1000-mb trough, then we would expect that the tropospheric mean temperature trough is doing likewise. For our case, the data in table 1 indicate that the 250-mb trough is overtaking the 1000-mb counterpart at the rate of about 5 m/s.

To explore the occlusion properties of the model, even through this approach, is not simple because from eq (22) and (23) it is evident that the 250-mb trough speed depends on every parameter of the model. Without performing an exhaustive study, we have made some sample

calculations for the case of $\hat{T} = 5^{\circ}\text{C}$, $\hat{\phi}_{10} = 10^3 \text{ m}^2\cdot\text{s}^{-2}$, and $\eta_0/T_0\gamma = 2.8 \times 10^{-6} \text{ s}^{-1}$. The results are shown in figure 16 where we see that, for wavelengths shorter than about 3800 km, the upper troposphere trough is overtaking the 1000-mb system. For wavelengths approximating the value for maximum deepening (fig. 13), the overtaking rate is close to 5 m/s for a wide range of values of the meridional temperature gradient. From a comparison of figures 13 and 16, however, occlusion does not seem to be a prerequisite for deepening.

A final consideration is the intensification rate of the extremely important temperature perturbation. For examining the effect in terms of the tropospheric mean temperature, we need merely to obtain at the origin the tendency of the thickness of the layer from 1000 to 250 mb:

$$\chi(0, 0, 250) - \chi(0, 0, 1000) = [\hat{\chi}_2(250) - \hat{\chi}_2(1000)] \sin \frac{2\pi}{L} \lambda. \quad (39)$$

From the definition of $\hat{\chi}_2$, we find that

$$\begin{aligned} \hat{\chi}_2(250) - \hat{\chi}_2(1000) = & \frac{(2\pi/L)Ra\hat{\phi}_{10} \ln 2}{f_0} \\ & + \frac{\eta_0 a \hat{\phi}_{10}}{(2\pi/L)T_0\gamma} \left\{ (\alpha k + 1)q \left[\left(\frac{1}{4}\right)^{\alpha-1} - 1 \right] + 1 \right\}. \quad (40) \end{aligned}$$

From eq (39), we see that intensification (or weakening) of the temperature perturbation cannot occur if the 1000-

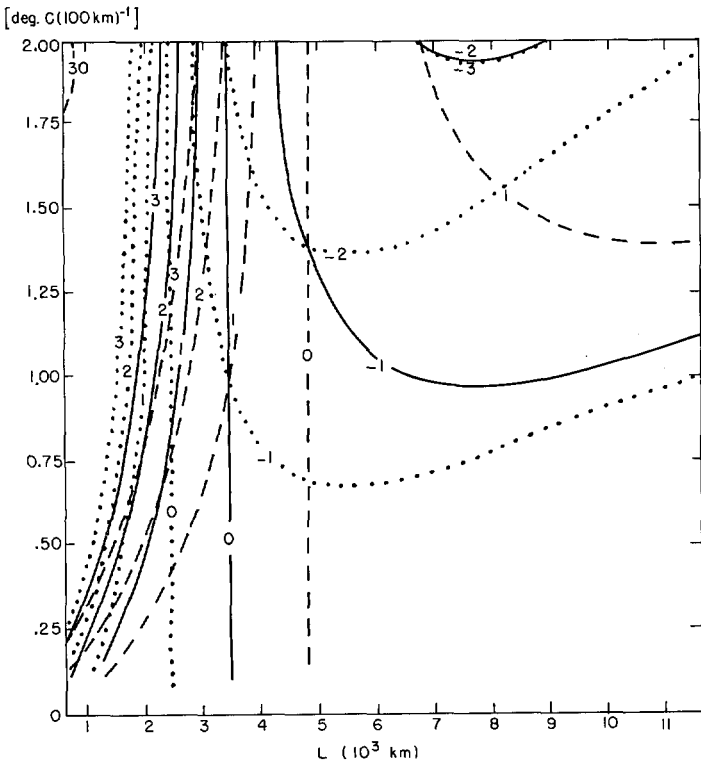


FIGURE 17.—Difference $\hat{\chi}_2$ at 250 mb minus $\hat{\chi}_2$ at 1000 mb for $\lambda=L/4$ as a function of wavelength and meridional temperature gradient for selected values of the vorticity-stability parameter. The dashed, solid, and dotted lines are as explained in figure 10. The isopleths are labeled in units of $10^{-2} \text{ m}^2 \cdot \text{s}^{-3}$. This difference represents the tropospheric mean temperature tendency at the cold perturbation center.

mb geopotential centers coincide with the centers of the temperature perturbation. Further, we see from eq (40) that there will probably be a critical wavelength below which intensification will not occur, because of the different dependence upon L shown by the two terms on the right side. It also is evident from eq (40) that, whether intensification or weakening is occurring, its intensity will be linearly proportional to a and to $\hat{\phi}_{10}$. These observations are confirmed in figure 17 that refers to the calculations with $a=10^{-5} \text{ }^\circ\text{C} \cdot \text{m}^{-1}$, $\hat{\phi}_{10}=10^3 \text{ m}^2 \cdot \text{s}^{-2}$, and $\eta_0/T_0\gamma=2.8 \times 10^{-6} \text{ s}^{-1}$. We see that, for wavelengths smaller than about 3500 km, the temperature perturbations are weakening, provided that $0 < \lambda < L/4$ (the usual state of affairs). In particular for the preferred wavelength shown in figure 13, the temperature perturbations are weakening at a rate somewhat in excess of $1^\circ\text{C}(12 \text{ hr})^{-1}$. These results are not strongly sensitive to variations in the vorticity-stability parameter. We are therefore left with something of a dilemma: the temperature perturbation is necessary for the deepening of the geopotential center, but this deepening simultaneously annihilates the perturbation, the origin of which is not clear. The theory is not much help, and we are not aware of any relevant observational studies.

8. CONCLUDING COMMENTS

In appraising our work, we have the impression that we have rediscovered baroclinic instability because our results are remarkably similar in many respects to those of Fjörtoft (1950), Charney (1947), and Eady (1949). In these classical studies, time-dependent solutions of linearized equations are obtained, while here we have only instantaneous solutions, but ones that pertain to the nonlinear situation. We are at a disadvantage because we must postulate the structure of the disturbance and cannot explain convincingly how it came to be. But we have the advantage of being able to compute detailed properties of the model, which appear realistic in most respects. We find, for example, an explanation for the tendency of surface cyclones to move to the right of the upper flow and the suggestion of an explanation for the failure of numerical prediction methods to forecast explosive cyclogenesis. It is true that we have found also a number of internal inconsistencies in the model, but these probably arise from nonlinear effects and would thus not be revealed by the linear analyses.

For some years now, the specific study of cyclones and anticyclones has been almost abandoned with the feeling that all questions would be answered in due course by generalized numerical prediction. As we find points of puzzlement in our theory, which underlies numerical prediction either explicitly or implicitly, we wonder whether the time is not "ripe" for re-examination of disturbances of synoptic scale from other points of view.

We feel, however, that the main significance of this work lies in the bridge it provides between the concepts that the synoptic meteorologist has traditionally employed and what appears to him to be the more esoteric notions of the theoretical meteorologist.

ACKNOWLEDGMENTS

The author wishes to express his gratefulness to Miss Colleen Leary of MIT (Massachusetts Institute of Technology) who programmed the numerous calculations and to Maj. H. J. E. Fischer, USAF (U.S. Air Force) who performed many of the computations. The work was supported in part by the Atmospheric Sciences Section, National Science Foundation, NSF Grant GA-10426.

REFERENCES

- Austin, J. M., "An Empirical Study of Certain Rules for Forecasting the Movement and Intensity of Cyclones," *Journal of Meteorology*, Vol. 4, No. 1 Feb. 1947, pp. 16-20.
- Charney, Jule G., "The Dynamics of Long Waves in a Baroclinic Westerly Current," *Journal of Meteorology*, Vol. 4, No. 5, Oct. 1947, pp. 135-162.
- Eady, E. T., "Long Waves and Cyclone Waves," *Tellus*, Vol. 1, No. 3, Stockholm, Sweden, Aug. 1949, pp. 33-52.
- Fjörtoft, Ragnar, "Application of Integral Theorems in Deriving Criteria of Stability for Laminar Flows and for the Baroclinic Circular Vortex," *Geofysiske Publikasjoner*, Vol. 17, No. 6, Oslo, Norway, Mar. 1950, 52 pp.
- Petterssen, Sverre, *Weather Analysis and Forecasting*, 2d Edition, Vol. 1, McGraw-Hill Book Co., Inc., New York, N.Y., 1956, 428 pp.
- Willett, Hurd Curtis, and Sanders, Frederick, *Descriptive Meteorology*, 2d Edition, Academic Press, New York, N.Y., 1959, 355 pp.